Attitude Estimation for a Flexible Spacecraft in an Unstable Spin

by Mark L. Psiaki[*], Eric M. Klatt[#], Paul M. Kintner, Jr.[**], and Steven P. Powell[##]

Cornell University, Ithaca, N.Y. 14853-7501

Abstract

An attitude reconstruction algorithm has been developed for a flexible sounding rocket whose spin vector nutates unstably about its minor inertia axis. This algorithm deduces attitude for use in post-flight analysis of the sounding rocket's science data. An additional motive for pursuing this work has been to show that a flexible-body dynamic model can be used in a Kalman filter/smoother-type attitude estimation system. The attitude reconstruction algorithm is a square-root information filter/smoother. It uses a dynamic model of the rocket that includes a main rigid body and a flexure mode for a pair of elastic booms. Boom bending is the principal cause of the energy loss that leads to unstable growth of the nutations. The flexure of the booms is modeled by a Markov process, but the laws of mechanics are used to model the flexure's influence on the attitude dynamics of the main spacecraft body. The filter/smoother achieves an attitude accuracy that is significantly better than can be achieved using a rigid-body model. The peak attitude error is estimated to be 4 deg, and the majority of the error seems to be caused by the limited accuracy of the rocket's attitude sensors.

---

[*] Associate Professor, Sibley School of Mechanical and Aerospace Engineering. Associate Fellow, AIAA.

[#] Graduate Student, School of Electrical Engineering.

[**] Professor, School of Electrical Engineering.

[##] Research Support Specialist, School of Electrical Engineering.

I. Introduction

The current work deals with the post-flight attitude determination for a sounding rocket mission, the Cleft Accelerated Plasma Experimental Rocket (CAPER). CAPER was launched from the Andoya Rocket Range in Norway in Jan. 1999. Its flight lasted slightly longer than 1,200 sec and reached an apogee altitude of 1360 km. The goal of this mission was to make measurements that would probe the behavior of the ionosphere during auroral events. One of these measurements was electric field. Attitude information was needed in order to properly resolve components of the measured electric field vector into geodetic coordinates. An attitude accuracy of 2 to 4 deg would be considered acceptable for the mission.

From an attitude determination standpoint, the important characteristics of the CAPER sounding rocket were as follows: Its attitude sensors were a vector sun sensor with a slit field of view (SS), a fixed-head horizon crossing indicator (HCI), and a 3-axis magnetometer that was mounted on a short boom. The rocket's attitude was passively spin stabilized with the nominal spin vector directed along its minor inertia axis. After exit from the atmosphere, CAPER deployed several booms. The longest of these were two flexible 3 m booms that deployed perpendicular to the nominal spin axis and in opposite directions from each other. A schematic diagram of this configuration appears in Fig. 1. CAPER's final stage rocket motor was spent before the time of interest; so, the system in question was a constant-mass system.

Minor axis spin stabilization is used often in sounding rocket experiments. Near the dawn of the space age, the Explorer-1 mission demonstrated that such a configuration has an unstable nutation mode due to energy dissipation in the flexible booms [1]. This instability is often accepted in sounding rocket experiment designs because of the ease of implementation of the system and because of the limited duration of the flight. It is allowable for the nutation mode to grow if the

resultant coning half angle does not become too large by the end of the flight.

The are two major challenges in doing post-flight attitude determination for the CAPER mission. The first is that there is no rate-gyro data. This means that some sort of Eulerian dynamics model has to be used in order to propagate the attitude and rates between measurement sample times. The model becomes especially important towards the end of the flight, when only magnetometer data is available. During this phase, the only other available attitude reference is the angular momentum vector, and its attitude reference accuracy depends heavily on the accuracy of the dynamic model. The second major challenge springs from the first: The rocket's attitude dynamics model contains two possible sources of significant error. One is uncertainty in the pre-launch reported values of the moments and products of inertia. The other is the presence of significant flexible motions of the booms that are shown in Fig. 1.

There is a significant body of research that is related to this attitude determination problem. A number of studies have been made of the dynamics and stability of non-rigid spinning spacecraft; see, for example, Ref. 2. They describe how dissipative flexible-body motions can cause nutation instability. Such studies are relevant to the development of a dynamical model for use in CAPER's attitude determination filter/smoother.

Other relevant works are those that deal with the general problem of spacecraft attitude determination. References 3-7 are good examples of this type of work. They all employ Kalman filters in one form or another in order to estimate attitude based on time series of attitude measurements. References 3 and 4 discuss traditional attitude determination filters, which propagate the attitude using rate gyros in order to avoid the use of uncertain dynamic models. References 5-7 are examples of a newer breed of attitude determination filters that do not use rate gyros. They explicitly include the attitude rates in the filter state and use Euler's equations to

propagate the estimates of these states.

The contribution of the current work is that it significantly extends the dynamic modeling of the newer filter design approach. These extensions are needed because of CAPER's instability. References 5-7 dealt with stable systems that experienced only small perturbations from a nominal state. CAPER, on the other hand, had a nutational instability that caused its coning half angle to grow from 20 deg at the beginning of the flight to over 75 deg at the end of the mission. Therefore, its attitude reconstruction filter/smoother will need a dynamic model that is accurate over a very large portion of the state space.

One new feature of the CAPER filter/smoother model is that it explicitly includes flexible-body dynamics. The filters of Refs. 5-7 all used rigid-body models. Reference 7 dealt with a spacecraft that had significant flexible-body motions due to launch damage, but it successfully modeled the flexible-body motions as those of a rigid body driven by random-walk torques. Unfortunately, the Ref.-7 approach has been found to work poorly for CAPER, which is why flexible-body dynamics have been explicitly included in its model.

Another new feature of the CAPER filter/smoother is that it explicitly estimates 5 of the 6 inertia parameters of the main rigid part of the spacecraft. The 6^{th} parameter is not observable. Estimation of these inertia matrix elements improves the fidelity of the dynamic model over the wide range of spin states that occurred during the CAPER mission.

Note that this paper deals with a smoothing problem. It has this luxury because its task is to perform attitude reconstruction. Nevertheless, the main contributions of this paper should be equally applicable to the filtering case because of the close link between smoothing and filtering.

This paper's findings are presented in two main sections. Section 2 describes the attitude reconstruction smoother. Section 3 presents the attitude determination results that have been

obtained using this smoother. It also compares the results with those of a Ref.-7-type smoother. Section 4 summarizes the main conclusions.

II. Smoother Design

General Smoother Problem Statement

A sampled data square root information filter/smoother (SRIF/S) has been chosen as the means of reconstructing CAPER's attitude time history. It is an extension to the nonlinear case of the covariance smoother of Ref. 8. This smoother starts with a forward SRIF filtering pass and follows it with a backwards covariance smoother pass. The extended algorithm is described in Ref. 7. It approximately solves a problem of the form:

Find: $\boldsymbol{x}_j$ and $\boldsymbol{u}_j$ for $j = 0, ..., N$ and $\boldsymbol{w}_j$ for $j = 0, ..., (N\text{-}1)$ (1a)

to minimize: $$J = \tfrac{1}{2}\{\sum_{j=0}^{N-1}\left\|R_{w(j)}\boldsymbol{w}_j - \boldsymbol{z}_{w(j)}\right\|^2 + \sum_{j=0}^{N}\left\|R_{u(j)}\boldsymbol{u}_j - \boldsymbol{z}_{u(j)}\right\|^2 + \left\|\tilde{R}_0\boldsymbol{x}_0 - \tilde{\boldsymbol{z}}_0\right\|^2\}$$ (1b)

subject to: $$\boldsymbol{x}_{j+1} = \boldsymbol{f}_d(\boldsymbol{x}_j, \boldsymbol{w}_j, j) \quad \text{for } j = 0, ..., (N\text{-}1)$$ (1c)

$$0 = \boldsymbol{h}(\boldsymbol{x}_j, \boldsymbol{y}_j, j) + \boldsymbol{u}_j \quad \text{for } j = 0, ..., N$$ (1d)

In this model form, $\boldsymbol{x}_j$ is the state vector at sample time t_j, $\boldsymbol{w}_j$ is the process noise that acts from sample time t_j to t_{j+1}, $\boldsymbol{y}_j$ is the measurement vector at time t_j, and $\boldsymbol{u}_j$ is the residual measurement error at time t_j. The discrete-time dynamics are defined by the vector function $\boldsymbol{f}_d(\boldsymbol{x}_j, \boldsymbol{w}_j, j)$ in difference equation (1c). The measurement model is defined implicitly by the function $\boldsymbol{h}(\boldsymbol{x}_j, \boldsymbol{y}_j, j)$ in measurement equation (1d).

This smoother is a maximum likelihood estimator. The square nonsingular matrices $R_{w(j)}$, $R_{u(j)}$, and $\tilde{R}_0$ and the vectors $\boldsymbol{z}_{w(j)}$, $\boldsymbol{z}_{u(j)}$, and $\tilde{\boldsymbol{z}}_0$ are used to define the least squares cost function in eq. (1b). These quantities also constitute a model of the *a priori* statistics of the

process noise, the measurement error, and the initial state: $\boldsymbol{w}_j \sim \mathrm{N}\{ R_{w(j)}^{-1}\boldsymbol{z}_{w(j)},\ R_{w(j)}^{-1}[R_{w(j)}^{-1}]^T \}$, $\boldsymbol{u}_j \sim \mathrm{N}\{ R_{u(j)}^{-1}\boldsymbol{z}_{u(j)},\ R_{u(j)}^{-1}[R_{u(j)}^{-1}]^T \}$, and $\boldsymbol{x}_0 \sim \mathrm{N}\{ \tilde{R}_0^{-1}\tilde{\boldsymbol{z}}_0,\ \tilde{R}_0^{-1}[\tilde{R}_0^{-1}]^T \}$, where the notation $\boldsymbol{q} \sim \mathrm{N}\{\boldsymbol{v},P\}$ indicates that $\boldsymbol{q}$ is a sample from a multivariate normal distribution whose mean is $\boldsymbol{v}$ and whose covariance is P. This problem model assumes that the random vectors $\boldsymbol{w}_j$, $\boldsymbol{u}_j$, and $\boldsymbol{x}_0$ are uncorrelated in time and uncorrelated with each other. The smoothed estimate minimizes the sum of the weighted square errors between $\boldsymbol{w}_j$, $\boldsymbol{u}_j$, and $\boldsymbol{x}_0$ and their *a priori* expectation values.

The dynamics function $\boldsymbol{f}_d(\boldsymbol{x}_j, \boldsymbol{w}_j, j)$ that appears in the discrete-time difference equation is defined via numerical solution of the following continuous-time initial value problem:

$$\dot{\bar{\boldsymbol{x}}}(t) = \boldsymbol{f}_c[\,\bar{\boldsymbol{x}}(t), \boldsymbol{w}_j, t] \qquad \text{for } t_j \le t < t_{j+1} \tag{2a}$$

$$\bar{\boldsymbol{x}}(t_j) = \boldsymbol{x}_j \tag{2b}$$

The discrete-time function $\boldsymbol{f}_d(\boldsymbol{x}_j, \boldsymbol{w}_j, j)$ is defined as $\bar{\boldsymbol{x}}(t_{j+1})$, the solution of the initial value problem at time t_{j+1}. The Runge-Kutta technique is used to solve this initial value problem.

The CAPER attitude reconstruction problem can be modeled in this form. The function $\boldsymbol{f}_c[\,\bar{\boldsymbol{x}}(t), \boldsymbol{w}_j, j]$ is defined using a flexible-body attitude dynamics model and a colored noise model of process disturbances. The elements of the vector function $\boldsymbol{h}(\boldsymbol{x}_j, \boldsymbol{y}_j, j)$ are chosen to model the three attitude sensors, the sun sensor, the horizon crossing indicator, and the magnetometer. The matrices $R_{w(j)}$, $R_{u(j)}$, and $\tilde{R}_0$ and the vectors $\boldsymbol{z}_{w(j)}$, $\boldsymbol{z}_{u(j)}$, and $\tilde{\boldsymbol{z}}_0$ are chosen partially based on the expected levels of random uncertainty and partially by tuning in order to get a solution that looks reasonable.

Smoother State Vector

CAPER's smoother state vector is

$$\boldsymbol{x} = [w; \boldsymbol{q}; a; \dot{a}; DI_{xx}; DI_{xy}; DI_{xz}; DI_{yy}; DI_{yz}; \boldsymbol{n}_{in}; Dh_{HCI}; \boldsymbol{b}_{bias}] \quad (3)$$

It has 21 elements. The first 3 elements are the vector w, the inertial spin rate expressed in a coordinate system that is fixed to the main rigid part of CAPER. This coordinate system is the one that is depicted by the *x*, *y*, and *z* axes in Fig. 1. The nominal spin axis is the *z* axis. Throughout the remainder of this paper, this coordinate system will be referred to as the body-fixed or spacecraft-fixed coordinate system. The normalized attitude quaternion $\boldsymbol{q}$ constitutes elements 4 through 7 of the state vector. It parameterizes the coordinate transformation from inertial coordinates to body-fixed coordinates.

The next two elements of the state vector come from the flexible-body part of the CAPER dynamics model. The 8th state vector element is a, the effective articulation angle of the flexible booms. The effective articulation is single-degree-of-freedom rotation about the $\hat{v}_{1b}$ axis; this axis is perpendicular to both the nominal boom direction and the nominal spin direction. a and $\hat{v}_{1b}$ are depicted on Fig. 1. The 9th state vector element, is $\dot{a}$.

The next 5 elements of the state vector, DI_{xx}, DI_{xy}, DI_{xz}, DI_{yy}, and DI_{yz}, are perturbations of inertia matrix elements for the main spacecraft body. There are perturbations for every independent element of the inertia matrix except for the nominal spin axis inertia.

The 15th through 17th elements of the state vector constitute the random-walk disturbance torque vector $\boldsymbol{n}_{in}$. This disturbance vector is defined in inertial coordinates.

The remaining elements of the state vector are sensor biases. The horizon crossing indicator's trigger height bias, Dh_{HCI}, is the 18th element of the state vector. The magnetometer's bias vector, $\boldsymbol{b}_{bias}$, constitutes the last 3 elements of the state vector.

Dynamics Model

The CAPER dynamics model consists of a set of differential equations that define the vector function $\boldsymbol{f}_c(\boldsymbol{x}, \boldsymbol{w}, t)$, which appears in eq. (2a). Some of these equations are based on physics. Others constitute statistical models of random processes. The differential equation for the first three elements of $\dot{\boldsymbol{x}}$ is a generalization of Euler's rigid-body attitude dynamics equation. It includes the effects of flexible motion of the booms:

$$\dot{w} = I_{tot}^{-1} \{ -2m_{tip} l_{tip}^2 \hat{\boldsymbol{v}}_{1b} \ddot{a} - \dot{I}_{tot} w - w \times [I_{tot} w + 2m_{tip} l_{tip}^2 \hat{\boldsymbol{v}}_{1b} \dot{a}] + \boldsymbol{n}_{gg}(\boldsymbol{q}, \boldsymbol{r}_{in}, I_{tot}) + A_{sc/in}(\boldsymbol{q})\, \boldsymbol{n}_{in} + \boldsymbol{w}_{sc} \} \quad (4)$$

This equation derives from the fact that the inertial rate of change of the angular momentum vector equals the net applied torque. The matrix I_{tot} is the total inertia of the main rigid body plus the flexible booms. It is computed about the system center of mass and is expressed in body-fixed coordinates. The quantities m_{tip} and l_{tip} are, respectively, the tip mass and length of each of the flexible booms. The vector function $\boldsymbol{n}_{gg}(\boldsymbol{q}, \boldsymbol{r}_{in}, I_{tot})$ is the gravity gradient torque, which depends on the attitude quaternion, the inertial position of the spacecraft in Earth-centered coordinates, $\boldsymbol{r}_{in}$, and the spacecraft total inertia. The matrix $A_{sc/in}(\boldsymbol{q})$ is the orthonormal transformation matrix from inertial coordinates to body-fixed coordinates. Its dependence on $\boldsymbol{q}$ is defined in Ref. 1, except that in the present implementation $\boldsymbol{q}$ always gets re-normalized before being used to compute $A_{sc/in}$. The vector $\boldsymbol{w}_{sc}$ is a white-noise process disturbance torque that is expressed in body-fixed axes.

The total spacecraft inertia can be computed by considering the geometry of Fig. 1. This computation uses unit vectors $\hat{\boldsymbol{v}}_{1b}$, $\hat{\boldsymbol{v}}_{2b}$, and $\hat{\boldsymbol{v}}_{3b}$. The direction $\hat{\boldsymbol{v}}_{2b}$ lies along the nominal boom direction. It is perpendicular to $\hat{\boldsymbol{v}}_{1b}$. The direction $\hat{\boldsymbol{v}}_{3b}$ is defined by the right-hand rule: $\hat{\boldsymbol{v}}_{3b} = \hat{\boldsymbol{v}}_{1b} \times \hat{\boldsymbol{v}}_{2b}$. Given these definitions, the total inertia is

$$I_{tot} = I_{rb} + \begin{bmatrix} DI_{xx} & DI_{xy} & DI_{xz} \\ DI_{xy} & DI_{yy} & DI_{yz} \\ DI_{xz} & DI_{yz} & 0 \end{bmatrix} + 2m_{tip}l_{tip}^2 [\,\hat{\boldsymbol{v}}_{1b}\hat{\boldsymbol{v}}_{1b}^T + \sin^2\!\boldsymbol{a}\ \hat{\boldsymbol{v}}_{2b}\hat{\boldsymbol{v}}_{2b}^T$$

$$- \sin\boldsymbol{a}\cos\boldsymbol{a}\,(\hat{\boldsymbol{v}}_{2b}\hat{\boldsymbol{v}}_{3b}^T + \hat{\boldsymbol{v}}_{3b}\hat{\boldsymbol{v}}_{2b}^T) + \cos^2\!\boldsymbol{a}\ \hat{\boldsymbol{v}}_{3b}\hat{\boldsymbol{v}}_{3b}^T\,] \qquad (5)$$

where I_{rb} is the nominal inertia that the spacecraft would have if l_{tip} were 0. It is expressed in body-fixed coordinates about the system center of mass. The time derivative $\dot{I}_{tot}$ can be derived from eq. (5) by using the chain rule while noting that $\boldsymbol{a}$ is the only time-varying quantity.

Equation (4) includes two random disturbance torque terms, $A_{sc/in}(\boldsymbol{q})\boldsymbol{n}_{in}$ and $\boldsymbol{w}_{sc}$. The first is a random-walk torque, and the second is a white-noise torque. Similar terms appear in the smoother model of Ref. 7. There are two main differences between these random torques and those of Ref. 7. The first is that the assumed intensities of these torques are much lower, relative to the spacecraft size, than those of Ref. 7. In other words, much less random torque is allowed as a way of fitting the measured CAPER data. The other difference is that Ref. 7 included a body-referenced random-walk torque, but the current model does not. Instead, it estimates inertia matrix perturbations, DI_{xx}, DI_{xy}, DI_{xz}, DI_{yy}, and DI_{yz}. This alternative approach achieves similar effects, but in a way that is physically more realistic.

The attitude kinematics yields an equation for the time derivatives of the 4th through 7th elements of the state vector [1]:

$$\dot{\boldsymbol{q}} = \frac{1}{2}\begin{bmatrix} 0 & w_z & -w_y & w_x \\ -w_z & 0 & w_x & w_y \\ w_y & -w_x & 0 & w_z \\ -w_x & -w_y & -w_z & 0 \end{bmatrix}\boldsymbol{q} \qquad (6)$$

where w_x, w_y, and w_z are the three body-fixed components of the spin rate vector, w.

The boom's rotational articulation motions are modeled by a second-order Markov process:

$$\ddot{a} = -a_1 \dot{a} - a_2 a + w_a \tag{7}$$

where a_1 and a_2 are constants that define the time correlation of the process, and w_a is the white-noise input that drives the process. This model is not based on physics.

It would be possible to develop a physical model for the time evolution of a. The model would be based on a single boom flexure mode. It would look very much like eq. (7), except that a_1 and a_2 would be determined by the boom's damping and bending stiffness, and there would be additional forcing terms involving w and $\dot{w}$ due to centrifugal, Coriolis, and angular acceleration effects.

A physics-based boom articulation model has not been used because of large uncertainty in the boom's damping. The Markov model allows the smoother to use the data rather than physics to determine reasonable boom motions. The resulting a time history can be checked to see whether it seems reasonable based on a physical model of the system.

The dynamic models for the rates of the remaining elements of the state vector, elements 10 through 21, are as follows:

$$D\dot{I}_{xx} = D\dot{I}_{xy} = D\dot{I}_{xz} = D\dot{I}_{yy} = D\dot{I}_{yz} = 0 \tag{8a}$$

$$\dot{\boldsymbol{n}}_{in} = \boldsymbol{w}_n \tag{8b}$$

$$D\dot{h}_{HCI} = 0 \tag{8c}$$

$$\dot{\boldsymbol{b}}_{bias} = 0 \tag{8d}$$

In other words, all of the remaining state vector elements are modeled as being constants, except for $\boldsymbol{n}_{in}$. It is modeled as being a random-walk vector whose time evolution is driven by the white process noise vector $\boldsymbol{w}_n$.

The general process noise vector that appears in problem (1a)-(1d), $\boldsymbol{w}$, can be defined in

terms of the white-noise process disturbances that appear in eqs. (4), (7), and (8b):

$$\boldsymbol{w} = [w_a; \boldsymbol{w}_n; \boldsymbol{w}_{sc}] \tag{9}$$

It is a 7-dimensional vector.

Attitude Sensor Models

The mathematical models of the attitude sensors are expressed in the functional form $\boldsymbol{h}(\boldsymbol{x}_j, \boldsymbol{y}_j, j)$ that appears in eq. (1d). This function compares the measured attitude data, $\boldsymbol{y}$, with what the model predicts based on the estimated state vector, $\boldsymbol{x}$. Each element of $\boldsymbol{h}(\boldsymbol{x}_j, \boldsymbol{y}_j, j)$ is a measure of the agreement between the model and the data. Perfect agreement is indicated when $\boldsymbol{h}(\boldsymbol{x}_j, \boldsymbol{y}_j, j)$ returns zeros [7].

Sun Sensor Model. The sun sensor is a slit-type device that digitizes a solar elevation angle whenever the sun passes through the plane of its slit. It produces a measured sun vector in spacecraft coordinates, $\hat{\boldsymbol{s}}_{meas/sc}$, approximately once per spin period. One can determine a modeled value of the sun unit vector in inertial coordinates, $\hat{\boldsymbol{s}}_{eph/in}$, from the solar ephemeris. Given these quantities, the sun-sensor elements of $\boldsymbol{h}(\boldsymbol{x}_j, \boldsymbol{y}_j, j)$ are

$$\boldsymbol{h}_{ss}(\boldsymbol{x}_j, \boldsymbol{y}_j, j) = \hat{\boldsymbol{s}}_{meas/sc} \times [A_{sc/in}(\boldsymbol{q})\ \hat{\boldsymbol{s}}_{eph/in}] \tag{10}$$

This vector defines the rotation needed to align the measured and modeled sun directions in spacecraft coordinates.

The expected raw accuracy of CAPER's sun sensor is about 1 deg. Its elevation digitization resolution is 2 deg, but the pixel intensity data admits finer interpolation. The sensor is uncalibrated, which is why its accuracy is so low. Two additional error sources are the Earth's albedo and the mounting alignment tolerance, which is on the order of 1 deg. The net measurement accuracy of this instrument has been modeled as being about 2 to 3 deg.

Horizon Crossing Indicator Model. The HCI is a narrow field-of-view telescope whose line of sight is fixed in the body frame. It measures the total received intensity in a radiation band that is emitted by atmospheric CO_2. Body axes rotation causes the telescope's line of sight vector to scan, and the detector's output undergoes sharp changes when it scans through the point of tangency to an ellipsoid that is approximately 40 km above the surface of the oblate Earth. The HCI's output data are the times of these abrupt changes in the signal level.

The HCI's $\boldsymbol{h}(\boldsymbol{x}_j, \boldsymbol{y}_j, j)$ element is defined by the tangency condition. The mathematical model for the tangency condition uses a weighting matrix to deal with the Earth's oblateness: $P = \text{diag}\{1, 1, [(r_{eq}+40\text{km}+Dh_{HCI})/(r_{po}+40\text{km}+Dh_{HCI})]\}$, where r_{eq} is the equatorial Earth radius, and r_{po} is the polar Earth radius. The model also uses two vectors that are weighted by this matrix: $\boldsymbol{r}_w = P\,\boldsymbol{r}_{in}$, and $\boldsymbol{v}_w = P\,A_{sc/in}^T(\boldsymbol{q})\,\hat{\boldsymbol{v}}_{HCI/sc}$, where $\hat{\boldsymbol{v}}_{HCI/sc}$ is the unit vector that points along the HCI line of sight in body-fixed coordinates. Recall that $\boldsymbol{r}_{in}$ is the inertial spacecraft position relative to the Earth, which is supplied by an on-board GPS receiver. Given these definitions, the HCI part of the $\boldsymbol{h}(\boldsymbol{x}_j, \boldsymbol{y}_j, j)$ function is

$$\boldsymbol{h}_{HCI}(\boldsymbol{x}_j, \boldsymbol{y}_j, j) \;=\; \begin{cases} [(r_{eq}+40km+Dh_{HCI})^2 - \boldsymbol{r}_w^T\,(I - \dfrac{\boldsymbol{v}_w\boldsymbol{v}_w^T}{\boldsymbol{v}_w^T\boldsymbol{v}_w})\boldsymbol{r}_w] & \text{if } \boldsymbol{v}_w^T\boldsymbol{r}_w < 0 \\ [(r_{eq}+40km+Dh_{HCI})^2 - \boldsymbol{r}_w^T\boldsymbol{r}_w] & \text{if } 0 \le \boldsymbol{v}_w^T\boldsymbol{r}_w \end{cases} \tag{11}$$

In practice, the condition $0 \le \boldsymbol{v}_w^T\boldsymbol{r}_w$ should never occur unless the measurement error is extremely large, which means that the lower line of this formula should never apply.

The accuracy of this attitude measurement depends on the uncertainty in the trigger height. Trigger height uncertainty can result from two sources. One is a height variation of the Earth's atmosphere as a function of the season and the local time of the point of tangency [9]. Additional uncertainty comes from the way that the detector's raw intensity data gets translated into a time of

tangency. A simple approach has been used: tangency is considered to occur when the detected intensity reaches 50% of its maximum value. Data analysis shows that the resulting trigger height random errors may be as large as 70 km. This translates into a 0.9 deg attitude measurement error at CAPER's 1360 km apogee altitude and a 1.7 deg error at the lowest altitude of interest, 420 km.

Magnetometer Model. The magnetometer is a 3-axis flux gate device. Its output is the measured magnetic field vector in spacecraft coordinates, $\boldsymbol{b}_{sc/mes}$. It is given in units of Tesla. It can be used as an attitude reference by comparing it with the known inertial magnetic field, which comes from a model [1, 10]. If the modeled inertial field is $\boldsymbol{b}_{in/mod}(\boldsymbol{r}_{in},t)$, then the mathematical model of the magnetometer part of $\boldsymbol{h}(\boldsymbol{x}_j, \boldsymbol{y}_j, j)$ is:

$$\boldsymbol{h}_{MAG}(\boldsymbol{x}_j, \boldsymbol{y}_j, j) = (\boldsymbol{b}_{sc/mes} - \boldsymbol{b}_{bias}) - A_{sc/in}(\boldsymbol{q})\, \boldsymbol{b}_{in/mod}(\boldsymbol{r}_{in},t) \tag{12}$$

This is a simple difference between the modeled field and the measured field, in spacecraft coordinates, after the estimated bias states have been subtracted off of the measured field.

There are various sources of error in the magnetometer data. Errors from spacecraft-generated fields are low due to the sensor's location on a boom. Similarly, errors due to resolution and mis-calibration are all low, under 6 nT (nano Tesla). The dominant errors come from the sensor's loose orthogonality and alignment requirements, only ± 1 deg, from uncertainty in the Earth's magnetic field model, and from disturbances to the field. These errors could add up to 1,000 nT. For the field magnitude range experienced during the flight, 32,000 to 46,000 nT, these error levels could translate into attitude measurement errors on the order of 1 to 2 deg.

Miscellaneous Smoother Details for CAPER Application

Attitude and Rate Initialization. Proper initialization of the smoother's attitude and attitude rate is very important due to the nonlinear nature of the extended estimation algorithm of Ref. 7. A poor initialization could lead to divergence during the forward filtering pass.

Initialization is accomplished as follows: First, the magnetic field time history is used to estimate the initial spin vector in spacecraft coordinates. The procedure neglects the slow inertial time variations of the magnetic field direction that are caused by the rocket's motion along its trajectory. This leads to the relationship $\dot{\hat{\boldsymbol{b}}}_{SC} = -w \times \hat{\boldsymbol{b}}_{SC} = \hat{\boldsymbol{b}}_{SC} \times w$, where $\hat{\boldsymbol{b}}_{SC}$ is the unit direction vector of the Earth's magnetic field as measured in spacecraft coordinates. The vector $\hat{\boldsymbol{b}}_{SC}(t)$ is available from the magnetometer (if one neglects biases), and $\dot{\hat{\boldsymbol{b}}}_{SC}(t)$ can be derived from $\hat{\boldsymbol{b}}_{SC}(t)$. If one uses this relationship at two different times that are approximately a quarter of a spin period apart, then one can derive a set of 6 linear equations in the 3 unknown elements of w. If the spin vector is not aligned with the field vector, then 4 of these 6 equations are linearly independent, and this over-determined set of equations can be solved in a least-squares sense to estimate w. The spin and field vectors are not aligned for the initial part of the CAPER data set; so, this technique works well.

Once the spin vector is known, the only remaining task is to estimate the initial attitude quaternion, $\boldsymbol{q}$. This is done by using two non-colinear unit direction vector observations, the normalized magnetic field vector and the sun direction vector. The initialization is carried out at an instant when both of these measurements are available.

All other elements of the state vector are assigned *a priori* values of zero at the initial time of the smoothing interval, t_0. Therefore, only the first 7 elements of the vector $\tilde{\boldsymbol{z}}_0$ are non-zero because these are the elements associated with the attitude and the spin rate.

Data Validation. Two simple checks have been performed in order to validate the sun sensor and magnetometer data. One quantity that has been checked is the magnitude of the measured magnetic field. It has been compared to the magnitude of the modeled field. The

maximum absolute difference between measured and modeled field magnitudes is 1,530 nT, and the maximum percentage difference is 4.2 %. This is without magnetometer bias estimation. With bias estimation, the maximum respective differences are 600 nT and 1.8 %. This low error level indicates that the magnetometer measurements are reliable.

The other data check has compared the measured and modeled values of the angle between the sun vector and the magnetic field vector. With compensation for magnetometer biases, the maximum angular discrepancy between the measurements and the model is 2.8 deg. This level of agreement is acceptable for CAPER's required attitude determination accuracy. It indicates that the attitude accuracy from the sun sensor, from the magnetometer, or from both is about 2 to 3 deg.

Data Editing. Some of the sun sensor and horizon crossing indicator data seemed to be invalid. Suspicious data points exhibited extremely large smoothed measurement residuals, $\boldsymbol{u}_j$. All such data points have been discarded. In total, 9 out of 235 HCI data points have been discarded as have 6 out of 98 sun sensor data points. All of the edited sun sensor points occurred after apogee, when CAPER's coning half angle had grown to more than 55 deg. At such large coning half angles the sun sensor sometimes had a problem with a high-reading/low-reading ambiguity in its output digitization map. The edited HCI data mostly occurred well before apogee. It is not clear what might have contributed to errors in these data points, except to say that there may have been a breakdown in the algorithm for deducing horizon crossing times from the recorded radiation intensity time history.

Sensor Alignment Estimation. Sometimes attitude determination filters or smoothers are used to estimate sensor misalignments, as in Ref. 7. In the present case, it was not considered to be worthwhile to try to estimate the relative misalignment between the sun sensor and the magnetometer. This decision was made because it is difficult, perhaps not even possible, to

accurately estimate this misalignment.

The one misalignment that has been estimated is that of the HCI bore sight vector as measured in spacecraft coordinates, $\hat{\boldsymbol{v}}_{HCI/sc}$. There were early indications that the reported direction of this vector could be in error by as much as 2 or 3 degrees. The misalignment of this vector has been estimated by using a batch process. The batch process makes use of the basic smoother. The smoother is run using a very high assumed HCI measurement uncertainty, which causes the algorithm to ignore the HCI data and use only magnetometer and sun sensor data in order to form its attitude estimate. This attitude estimate is then used to calculate HCI measurement errors, $\boldsymbol{h}_{HCI}(\boldsymbol{x}_j, \boldsymbol{y}_j, j)$. The vector $\hat{\boldsymbol{v}}_{HCI/sc}$ is then perturbed in two orthogonal directions, and the smoother is run two more times to determine the effect of $\hat{\boldsymbol{v}}_{HCI/sc}$ perturbations on the HCI measurement errors. Finally, this linearized model is used in a batch least-squares calculation to correct $\hat{\boldsymbol{v}}_{HCI/sc}$ in such a way that the corrected vector yields the minimum mean square HCI measurement error. This procedure has resulted in a 2.1 deg correction to the direction of $\hat{\boldsymbol{v}}_{HCI/sc}$.

Iterative Inertia Matrix Estimation and the Final Estimate. The smoother assumes nominal values for the 6 elements of I_{rb}, and it estimates perturbations to 5 of these parameters. The smoother's performance can be slightly influenced by large errors in the initial nominal values of inertia parameters. One influence comes from the nonlinearity of the smoother, and the other influence comes from the need to assign some non-infinite initial level of uncertainty to the 5 estimated perturbations.

An iterative inertia estimation process has been employed in order to minimize the impact of initial errors in the nominal values. This iterative process is simple: the smoother is first run using

design values for the nominal inertias. The next time the smoother is run, it uses new nominal values: the previous nominal values plus the estimated perturbations from the previous smoother run. This process has been iterated only 2 times, after which the estimated perturbations are all less than 1 % of the system's maximum principal inertia.

The final estimates of the nominal total system principal inertias are 211.73 kg-m^2, 190.84 kg-m^2, and 18.72 kg-m^2. The last quantity is the inertia about the nominal spin axis. These inertias include the effects of the booms, whose properties are l_{tip} = 3.24 m and m_{tip} = 0.4288 kg.

Smoother Tuning. The smoother gets tuned via selection of quantities that model various *a priori* error statistics. The matrix $\tilde{R}_0$ is initialized to reflect the estimation error covariances for the *a priori* initial state estimate, $\tilde{\boldsymbol{x}}_0 = \tilde{R}_0^{-1}\tilde{\boldsymbol{z}}_0$. Except for a modification in the quaternion terms, $\tilde{R}_0$ is a diagonal matrix. Each diagonal element is of the form $1/\boldsymbol{s}$, where $\boldsymbol{s}$ is an *a priori* state estimation error standard deviation. The *a priori* standard deviations are 16 deg/sec for each element of the spin vector, w, (20% of the initial spin rate), 15 deg for each independent direction of attitude uncertainty, 10 deg for the initial $\boldsymbol{a}$ uncertainty, 20 deg/sec for the initial $\dot{\boldsymbol{a}}$ uncertainty, 30 kg-m^2 for the initial DI_{xx} and DI_{yy} uncertainties, 10 kg-m^2 for the initial DI_{xy}, DI_{xz}, and DI_{yz} uncertainties, 0.0006 N-m for each element of the inertial random-walk disturbance vector, $\boldsymbol{n}_{in}$, 20,000 m for the HCI trigger height bias, Dh_{HCI}, and 3,000 nT for each element of the magnetometer bias vector, $\boldsymbol{b}_{bias}$. With the exception of the random-walk disturbance torques, these *a priori* standard deviations have been chosen to be as large as seemed practical. This has been done in order to minimize the effects of *a priori* assumptions on the final smoother solution. The possibility of filter/smoother divergence is what places practical maximum limitations on the sizes of these *a priori* standard deviations.

The measurement noise statistics have been modeled as follows: $\boldsymbol{z}_{u(j)}$ has been set equal to zero for all sample times because the measurement errors are assumed to have zero mean. The measurement error standard deviations are used to form the elements of the diagonal matrix $R_{u(j)}$. As with $\tilde{R}_0$, if s is the standard deviation of a particular measurement, then $1/s$ is the corresponding diagonal element of $R_{u(j)}$. The sun sensor measurement standard deviation was set to 5 deg per axis, the HCI s value was set to 132,000 m, and the magnetometer's random error component was modeled as having a standard deviation of 3,000 nT per axis.

The process noise statistical model defines the $\boldsymbol{z}_{w(j)}$ vector, the $R_{w(j)}$ matrix, and the values of a_1 and a_2 in the Markov model of the boom articulations. The vector $\boldsymbol{z}_{w(j)}$ has been set equal to zero, and the matrix $R_{w(j)}$ has been defined as follows:

$$R_{w(j)} = \text{diag}(1/s_{wa},\ 1/s_{wn},\ 1/s_{wn},\ 1/s_{wn},\ 1/s_{wsc},\ 1/s_{wsc},\ 1/s_{wsc})\sqrt{t_{j+1} - t_j} \tag{13}$$

where $s_{wa} = 48$ deg/sec$^{1.5}$, $s_{wn} = 6\times10^{-5}$ N-m/sec$^{0.5}$, and $s_{wsc} = 1.5\times10^{-3}$ N-m-sec$^{0.5}$.

The Markov process in eq. (7) is assigned an undamped natural frequency of 2 rad/sec and a damping ratio of 0.7071. Therefore, $a_1 = 2.8284$/sec and $a_2 = 4$/sec^2.

Smoother Tuning Process. The smoother has required a certain amount of tuning in order to arrive at the numbers given in the previous section. The important tuning parameters are the sensor accuracies that appear in inverse form in the $R_{u(j)}$ matrix and the process noise intensities whose inverses form the diagonal elements of $R_{w(j)}$. The magnetometer and sun sensor error standard deviations have been chosen to be about a factor of 2 larger than the error levels noted in the data validation section of this paper. The parameters of the boom articulation Markov model in eq. (7), a_1, a_2, and s_{wa}, have been chosen to give a bandwidth that is slightly higher than the nutation

frequency and a steady-state a standard deviation that is about 4 times larger than what is expected based on physical models. The remaining tuning parameters, the HCI measurement error standard deviation and the process noise intensities for the white-noise and random-walk torques, have been chosen by trial-and-error runs of the smoother.

Initially, the smoother used values of the HCI measurement error standard deviation and values of the process noise intensities that were larger than the final best values that are reported above. The initial trial value of the HCI noise standard deviation was 1.3 times the final best-case value, and the initial trial values of the process noise intensities s_{wn} and s_{wsc} were 33 times larger than the final values.

Smoothing runs were then attempted with successively lower values of these noise standard deviations until the final best-case values were determined. The goal was to use the lowest possible values for the HCI errors and the random torque intensities because it was believed that these error sources should be small. At some point, the smoother began to exhibit poor performance when very small values for these noise intensities were used. This poor performance was evident in the smoother's measurement error estimates: their time histories exhibited very large spikes. The final best-case tunings of these quantities have been selected as the smallest values that do not cause obvious large spikes in the smoothed measurement errors.

III. Attitude Determination Results

The smoother of Section II has been run on the actual data from the CAPER mission. Several different runs have been made. Also, comparison runs have been made using a smoother that uses only a rigid-body model and larger disturbance torques, like that of Ref. 7. Results of these runs are presented in this section.

Best-Case Smoother Performance

This sub-section discusses the smoother's performance under the best possible tunings, those that have been presented at the end of Section II.

The first plots to consider are those of the smoothed residual measurement errors. These are the values of elements of $\boldsymbol{h}(\boldsymbol{x}_j, \boldsymbol{y}_j, j)$, but re-scaled into sensible units. The sun sensor errors are plotted on the top plot of Fig. 2, the magnetometer errors on the bottom plot, and the HCI errors on Fig. 3. The sun sensor and magnetometer errors are both given in spacecraft coordinates. The magnetometer errors and the HCI errors have units called approximate degrees. In the case of the magnetometer, this means that the error in Tesla has been scaled by 180/(p*field magnitude). In the case of the HCI, the trigger height error in meters has been divided by the distance from the spacecraft to the trigger point and then multiplied by 180/p.

There are several significant points to notice about the smoothed measurement errors. First, there are no sun sensor or HCI measurement errors for the last 200 sec of the smoother run (from 300 sec to 500 sec after apogee). The large final coning angles of CAPER caused this loss of data. Second, all of these errors are of a reasonable size based on the modeled statistics. The sun sensor errors are all less than 3 deg, and most are less than 2.5 deg. The magnetometer errors are all less than 1.6 deg, and the HCI errors are all less than 1.5 deg. The third point is that the errors appear to have some correlation. The most striking correlations appear in the HCI errors of Fig. 3. Roughly speaking, the points of the figure can be described as forming a flattened "X." The upper-left to lower-right stroke of the "X" is formed primarily by in-crossings, i.e., by space-to-Earth scans of the horizon telescope, and the lower-left to upper-right branch of the "X" is formed primarily by out-crossings (Earth-to-space scans). The magnetometer errors show a different kind of correlation. Although not obvious on the scale of the plot due to the density of the points, there

is a periodicity to the errors that corresponds to the body-axis nutation period.

It is not clear why there are correlations in the smoothed measurement errors. The theory of smoothers says that there should be no such correlation if the system is perfectly modeled and if the error sources are truly random. Obviously, some of these assumptions are violated by the system. One possible source of the systematic errors is the loose orthogonality specification on the magnetometer axes and the lack of sun sensor calibration. Despite these problems, this performance is probably acceptable for the mission at hand. In any case, the attitude accuracy has been checked by an independent measurement, as will be discussed below.

The estimated spin vector time history for this case is shown in Fig. 4. As expected, the spin vector starts out mostly along the z axis, which is the nominal spin axis. As time progresses, the amplitude of the w_x-w_y nutations grows, and the magnitude of w_z decreases. At the end of the mission, the spin vector is about 20 deg away from the z axis. More importantly, the angular momentum vector is over 75 deg away from the z axis at the end of the mission. This latter angle is the observed coning half angle of the system, which means that CAPER was in a very flat spin at the end of its flight.

The boom articulation angle time history, $a(t)$, is shown in Fig. 5. This plot is roughly consistent with what physics would predict for the response of the booms. The primary boom response is an oscillation at the body-axes nutation frequency of the spin vector. The boom response lags behind the forcing that arises due to centrifugal effects and angular acceleration. This lag is what causes energy loss and the resultant growth of the nutation amplitude. The magnitude range of the oscillations, between 4 and 10 degrees peak-to-peak, is consistent with physics-based models for this system that include boom stiffness, first-mode boom bending in two planes, and all of the relevant spin-vector-induced interaction forces.

There is one strange part of Fig. 5: the amplitude "beats" that occur during the first 250 sec of the smoother run. There is no obvious explanation for these. They correspond to small transient energy oscillations in the system that seem to be unphysical. These beats may be caused by systematic measurement errors. The resultant anomalous motions are not very large; so, it is reasonable to ignore this problem.

The total external torque for this case is relatively low. The maximum magnitude of the total estimated random torque, max $\|A_{sc/in}(\boldsymbol{q})\, \boldsymbol{n}_{in} + \boldsymbol{w}_{sc}\|$, is 0.0011 N-m. Although small, this value is still at least one order of magnitude larger than the maximum expected levels of actual disturbance torques such as drag and solar radiation pressure. The only possible explanation for these residual torques is modeling error either in the dynamics or in the sensors.

The estimated torques do not cause the angular momentum vector to drift very much in inertial space. The magnitude of the angular momentum stays within 2.3% of its initial value, and the inertial orientation drifts by less than 1 deg, as shown in Fig. 6. A very important feature of Fig. 6 is the drift during the last 200 sec of the smoother run. As shown on Figs. 2 and 3, there is no sun sensor or HCI data during this time interval. This means that the system's only useable attitude references are the magnetic field and the angular momentum vector. The estimated angular momentum vector drifts by only 0.2 deg during this final phase of the smoothing run. Therefore, the estimated angular momentum can provide a useful second attitude reference during the last 200 sec of the flight.

The final plot to consider for the nominal smoother case is that of the estimated total kinetic energy. It is shown in Fig. 7. As expected, this plot shows a dramatic loss of energy as the flight progresses. This is the loss associated with nutation growth for a minor-axis spinner. It is caused by damping of the boom articulation oscillations.

Figure 7 indicates that there is a slight kinetic energy increase for the first 8 sec of the smoothing run. This is unphysical. It is interesting to note that this small wrinkle in the plot occurs at the same time that an anomalous boom articulation angle "beat" appears on Fig. 5. It is believed that both of these responses are the results of the same systematic modeling error.

Independent Attitude Check

The smoother's attitude estimates have been partially verified using independent data. This data comes from electric field probes that are mounted at the ends of the booms. These probes are known to experience voltage spikes when they pass through the rocket body's solar shadow. These shadowing times can be predicted based on the main spacecraft body's geometry and the smoother's attitude estimate. These predictions have been generated, and they have been compared to the times of the actual spikes in the probe voltage time histories. There are 161 observable spikes in the data. 136 of these match with predicted spikes. The other 25 data spikes were not predicted at all, probably due to approximation errors of the geometric shading model that was used to generate the predictions. The relevant spikes in the voltage time histories have been found to agree with the 136 predicted spikes to within 0.14 sec. If one multiplies the estimated spin rate by these timing errors, then they yield a maximum spacecraft orientation error of 3.9 deg. This shadowing data extends all the way to the end of the smoothing run. Therefore, these positive results verify that the smoother yields a reasonable attitude estimate even when sun sensor and HCI data are no longer available.

Conjecture about Factors that Limit the Attitude Accuracy

It is believed that the limiting factors in the accuracy of this example come from measurement errors in CAPER's attitude sensors. As seen in Figs. 2 and 3 and in the independent data consistency checks, the raw attitude measurement errors are on the order of 1 to 3 degrees. The

shading check demonstrates that the attitude solution has about the same level of accuracy. Furthermore, there seem to be systematic effects in the measurement errors. These systematic effects probably keep the smoother from using its averaging capabilities to achieve results that are more accurate than the raw sensor data. Therefore, it is believed that a much more accurate attitude solution could be achieved with this technique if higher-accuracy sensors were available.

Comparison with a Rigid-Body Based Smoother

The present results have been compared with a smoother like that of Ref. 7. It uses a rigid-body model of the spacecraft, and it allows larger disturbance torque estimates in order to try to account for various sources of modeling error, including flexible-body effects. It includes random-walk torques both in inertial axes and in body axes. The inertial torques account for any unmodeled precession of the angular momentum vector, and the body-axis torques account for effects such as principal axis modeling errors.

The CAPER results for this rigid-body type smoother are problematical. The estimated random torques are very large. They vary between 0.3 and 0.4 N-m for most of the run, and they spike up as high as 20 and 28 N-m during two anomalous parts of the smoothed solution. Even without the anomalous portions, the average estimated torques are about 300 times larger than for the smoother that uses a flexible-body model. Such large disturbance torques are totally inconsistent with the physics of the system.

Figure 8 gives a summary comparison between the two attitude estimation algorithms. It plots the total angular discrepancy between the flexible-body smoother's attitude estimate and that of the rigid-body smoother. The two smoothers agree fairly well up to about 100 sec after apogee. During this time period, full 3-axis attitude measurement data is available, and the coning half angle is less than 60 deg. The two attitude estimates are within 2 deg of each other during this

period, except for a small initial spike of 4.2 deg discrepancy.

The rigid-body-based smoother experiences serious problems starting at about 100 sec after apogee. These are evidenced by very large residual measurement errors and by spikes in the estimated spin vector. Figure 8 shows corresponding spikes in the attitude discrepancy between the two smoothers. These correspond to erroneous 360 deg rotations of the rigid-body smoother's attitude estimate. The bottom line on the rigid-body smoother is that it has problems in dealing with a sparse set of measurement data, a large coning half-angle, or both.

IV. Conclusions

This paper describes an attitude reconstruction smoother that has been applied to the CAPER sounding rocket mission. The achieved accuracy of the smoother is estimated to be about 4 deg per axis. This estimate is based on the level of the smoothed attitude measurement errors and on independent data: the solar shading times for boom-mounted electric field probes.

The smoother has two new features that are important to its success. First, it estimates corrections to 5 of the 6 independent elements of the inertia matrix of the main spacecraft body. Second, it explicitly incorporates a simple flexible-body model of the dominant elastic mode of a pair of booms. The energy loss in the boom deflections causes nutation growth because CAPER is a minor axis spinner. The estimated coning half angle grows from 20 deg at the start of the mission to over 75 deg by the end of the flight. The flexible-body model accurately captures this coning half angle growth. The smoother is able to accurately reconstruct attitude at the end of the flight despite the fact that CAPER's flat terminal spin causes some of the sensors to stop returning data.

Acknowledgment

This work was supported in part by NASA grant number NAG5-5079, Cleft Accelerated Plasma Experimental Rocket. The payload and rocket were designed and built at the NASA Goddard Space Flight Center, Wallops Flight Facility.

References

1. Wertz, J.R. ed., *Spacecraft Attitude Determination and Control*, D. Reidel Pub. Co., (Boston, 1978), pp. 414, 501-502, 512, 779-786.
2. Levinson, D.A. and Kane, T.R., "Spin Stability of a Satellite Equipped with Four Booms," *Journal of Spacecraft and Rockets*, Vol. 13, No. 4, 1976, pp. 208-213.
3. Lefferts, E.J., Markley, F.L., and Shuster, M.D., "Kalman Filtering for Spacecraft Attitude Estimation," *Journal of Guidance and Control*, Vol. 5, No. 5, 1982, pp. 417-429.
4. Rupp T. and Schneiders G., "High-Accuracy Attitude Determination for the X-Ray Satellite ROSAT," *Journal of Guidance, Control, and Dynamics*, Vol. 15, No. 3, 1992, pp. 554-561.
5. Psiaki, M.L., Martel, F., and Pal, P.K., "Three-Axis Attitude Determination via Kalman Filtering of Magnetometer Data", *Journal of Guidance, Control, and Dynamics*, Vol. 13, No. 3, 1990, pp. 506-514.
6. Axelrad, P., and Ward, L.M., "Spacecraft Attitude Estimation Using the Global Positioning System: Methodology and Results for RADCAL," *Journal of Guidance, Control, and Dynamics*, Vol. 19, No. 6, 1996, pp. 1201-1209.
7. Psiaki, M.L., Theiler, J., Bloch, J., Ryan, S., Dill, R.W., and Warner, R.E. “ALEXIS Spacecraft Attitude Reconstruction with Thermal/Flexible Motions Due to Launch Damage”, *Journal of Guidance, Control, and Dynamics*, Vol. 20, No. 5, 1997, pp. 1033-1041.

8. Bierman, G.J., *Factorization Methods for Discrete Sequential Estimation*, Academic Press, (New York, 1977), pp. 69-76, 115-122, 214-217.
9. Cowley, J.R., “Horizon Sensor Trigger Altitudes Derived from Apparent Pitch Variations of the Solar Mesosphere Explorer,” Paper No. AAS-87-493, American Astronautical Society, (Springfield, Virginia, Aug. 1987).
10. Anon., "DGRF/IGRF Geomagnetic Field Model 1945 - 2000 and Related Parameters," http://nssdc.gsfc.nasa.gov/space/model/models/igrf.html, National Space Science Data Center, NASA Goddard Space Flight Center, April, 1999.

Figure Captions

Fig. 1. CAPER sounding rocket configuration.

Fig. 2. Sun sensor and magnetometer residual measurement error time histories for the nominal smoother case.

Fig. 3. Horizon crossing indicator residual measurement error time history for the nominal smoother case.

Fig. 4. The estimated body-axes spin vector time history, $w(t)$, for the nominal smoother.

Fig. 5. Boom articulation angle time history, $a(t)$, for the nominal smoother.

Fig. 6. Time history of angle between instantaneous total angular momentum vector and its initial direction in inertial coordinates, nominal smoother case.

Fig. 7. Estimated total kinetic energy time history for the nominal smoother.

Fig. 8. Time history of the total attitude discrepancy between the nominal flexible-body smoother and the rigid-body smoother.

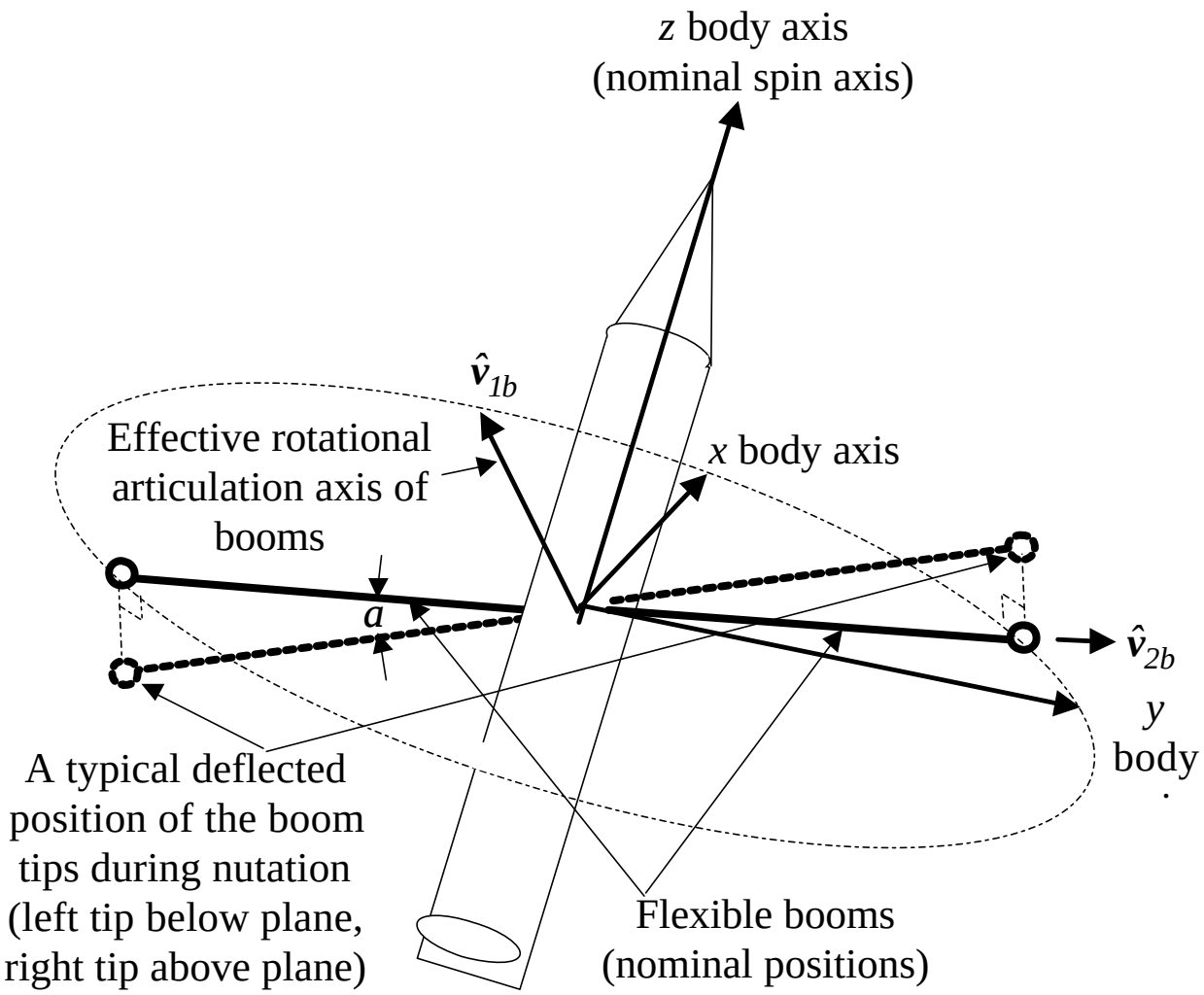

Fig. 1. CAPER sounding rocket configuration.

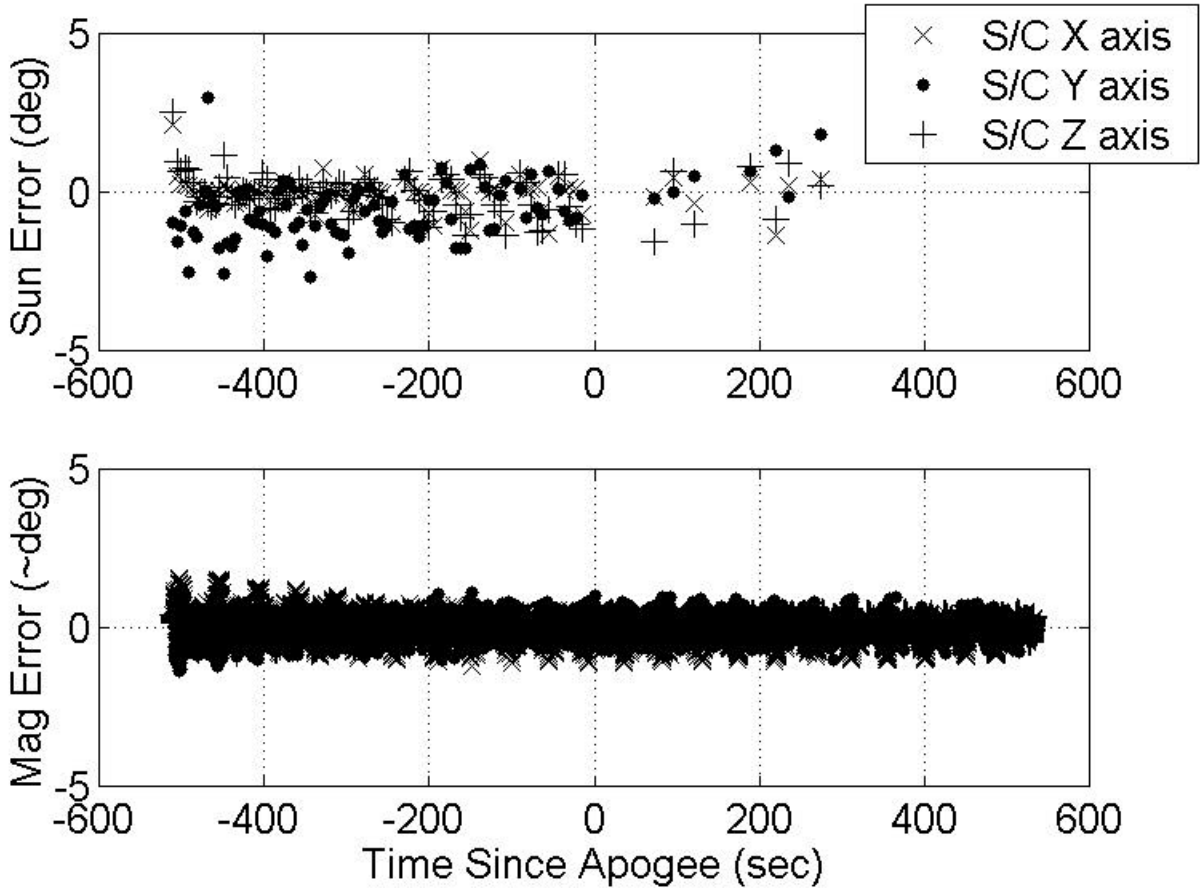

Fig. 2. Sun sensor and magnetometer residual measurement error time histories for the nominal smoother case.

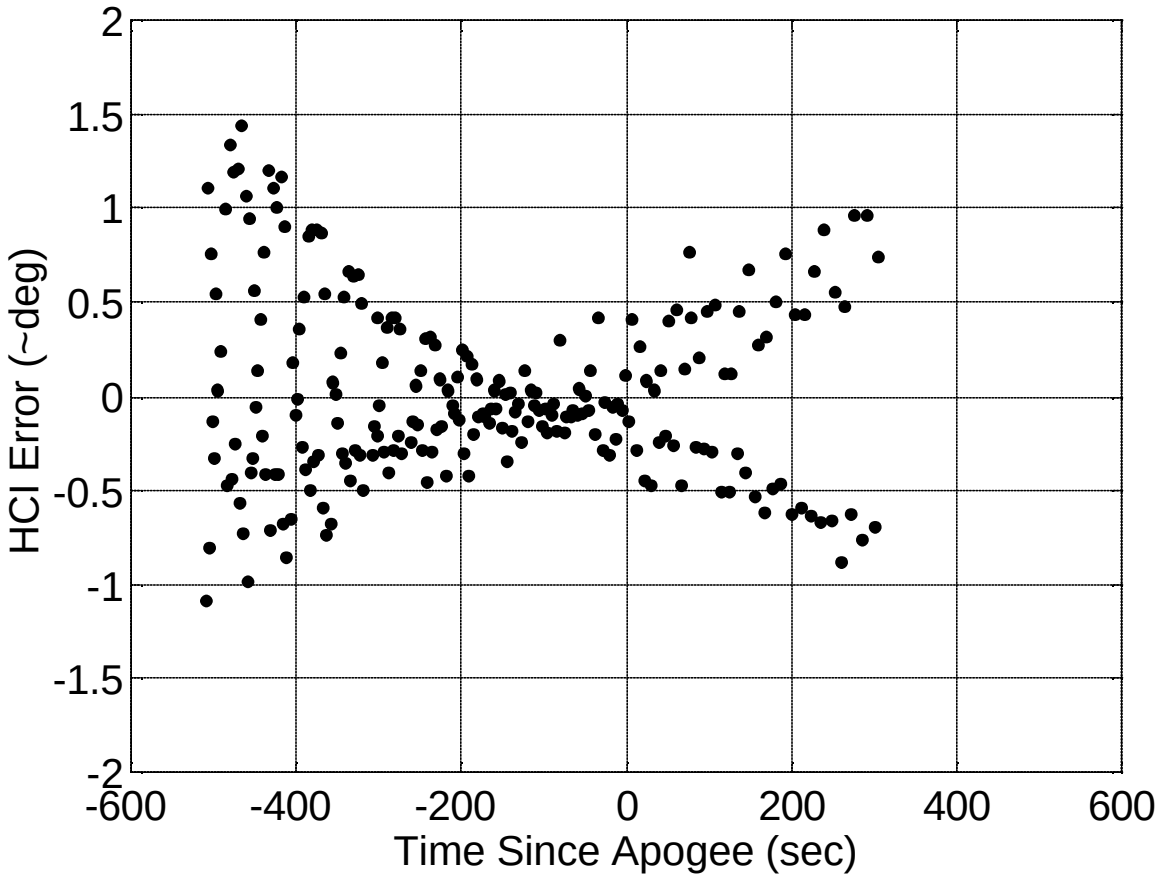

Fig. 3. Horizon crossing indicator residual measurement error time history for the nominal smoother case.

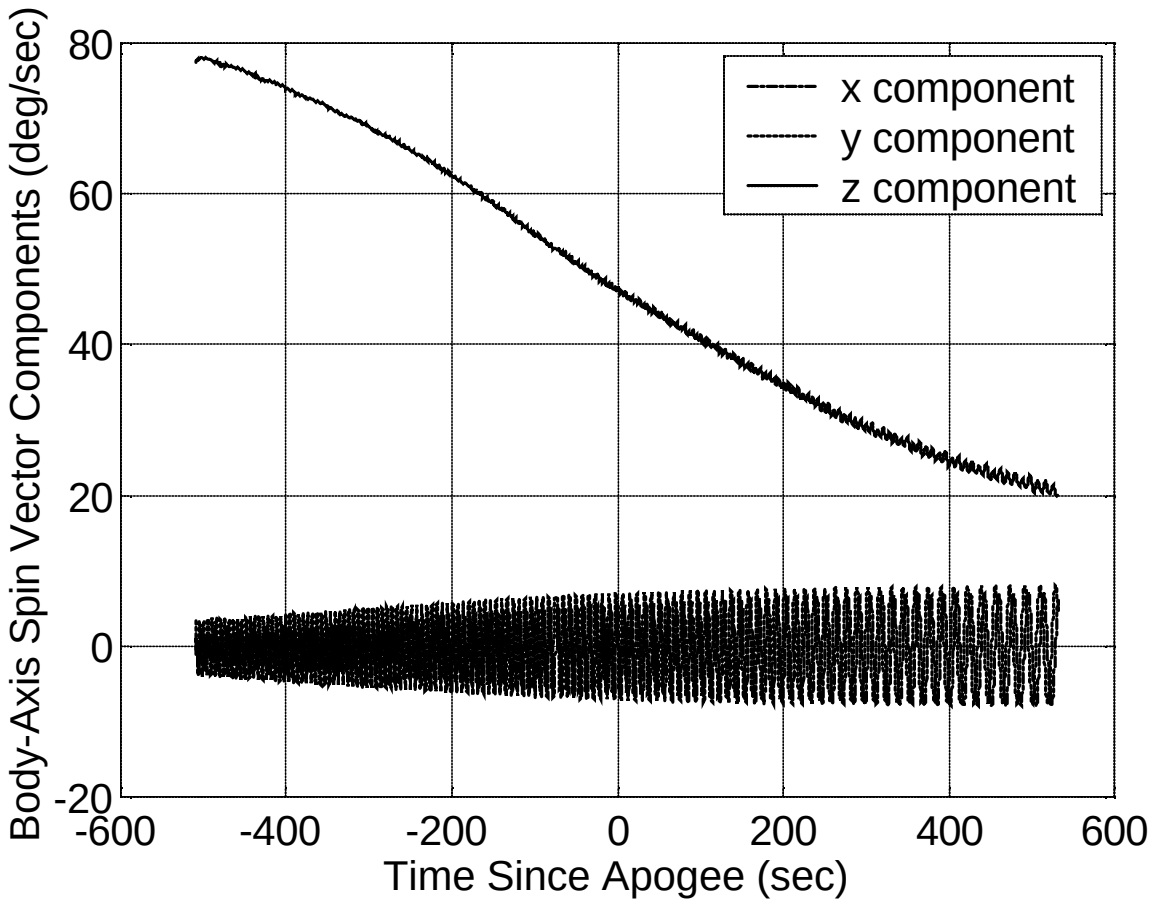

Fig. 4. The estimated body-axes spin vector time history, w(t), for the nominal smoother.

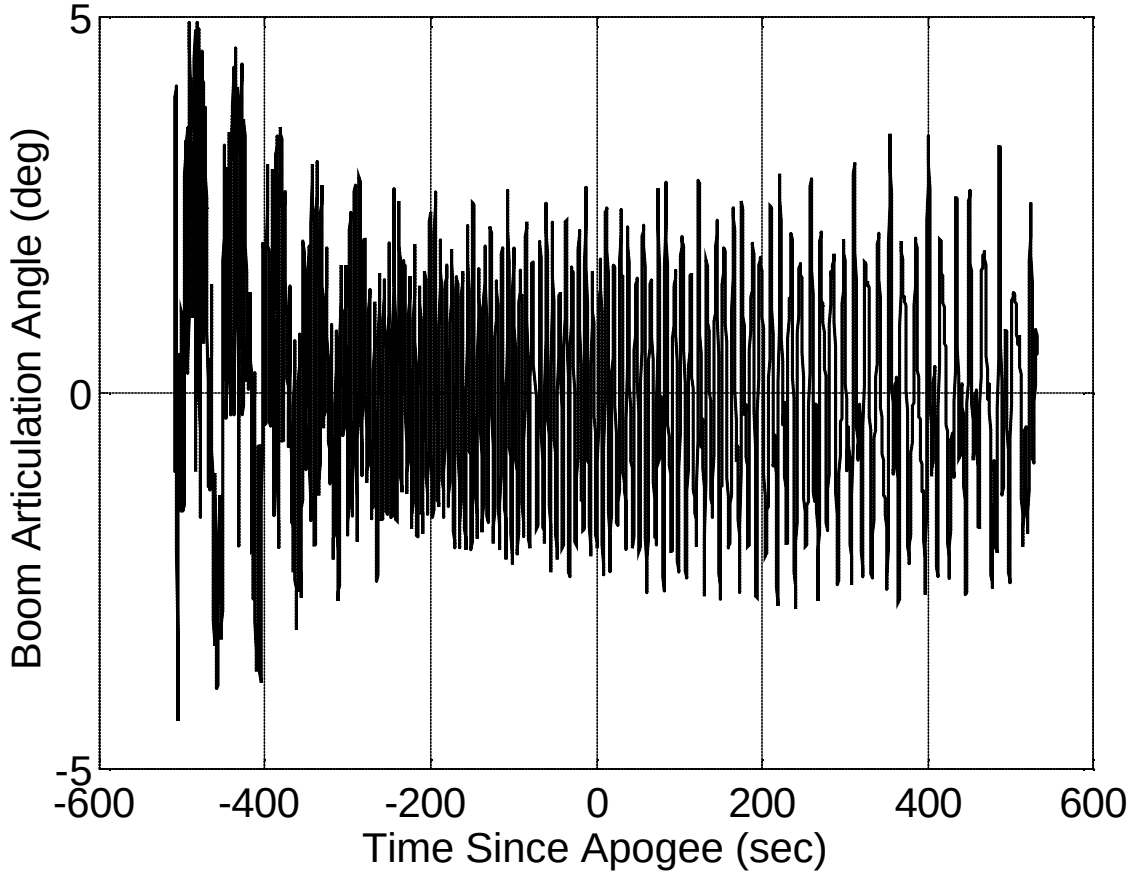

Fig. 5. Boom articulation angle time history, a(t), for the nominal smoother.

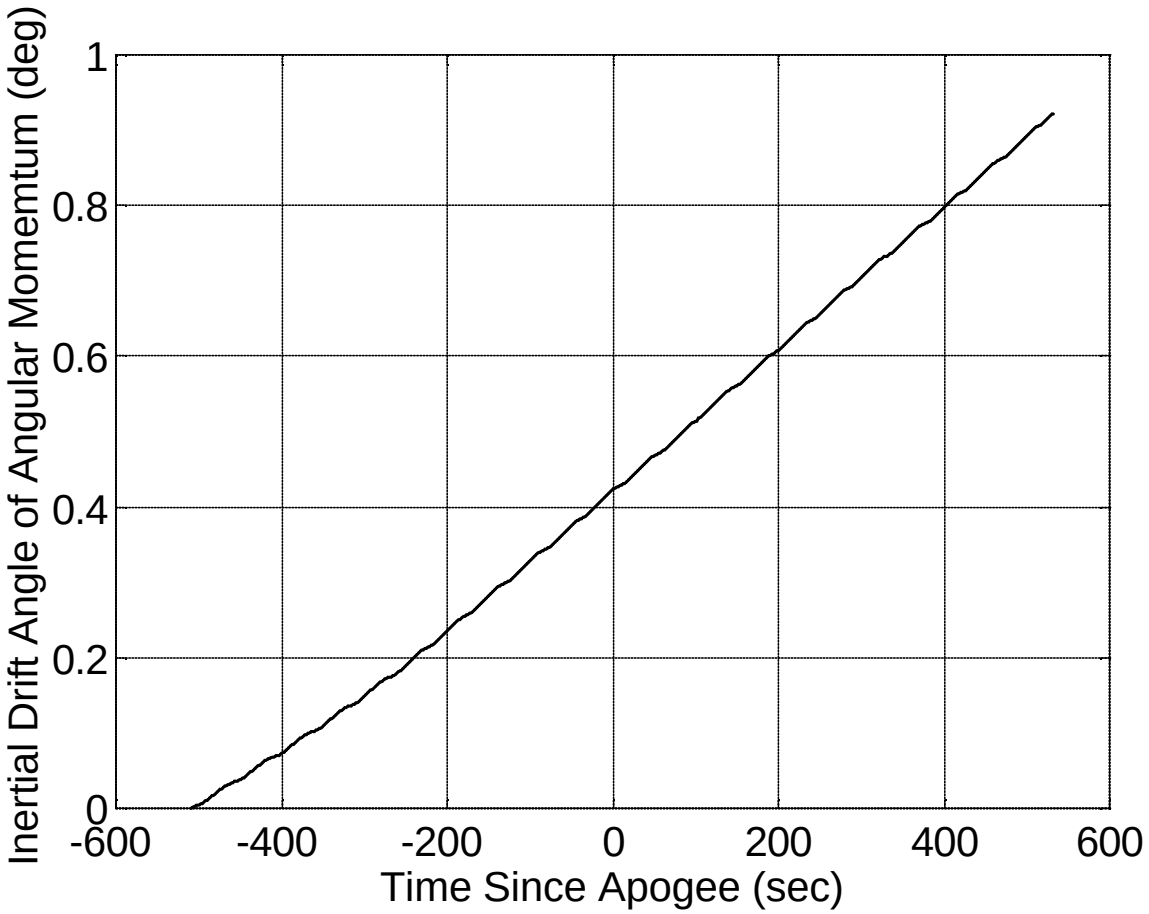

Fig. 6. Time history of angle between instantaneous total angular momentum vector and its initial direction in inertial coordinates, nominal smoother case.

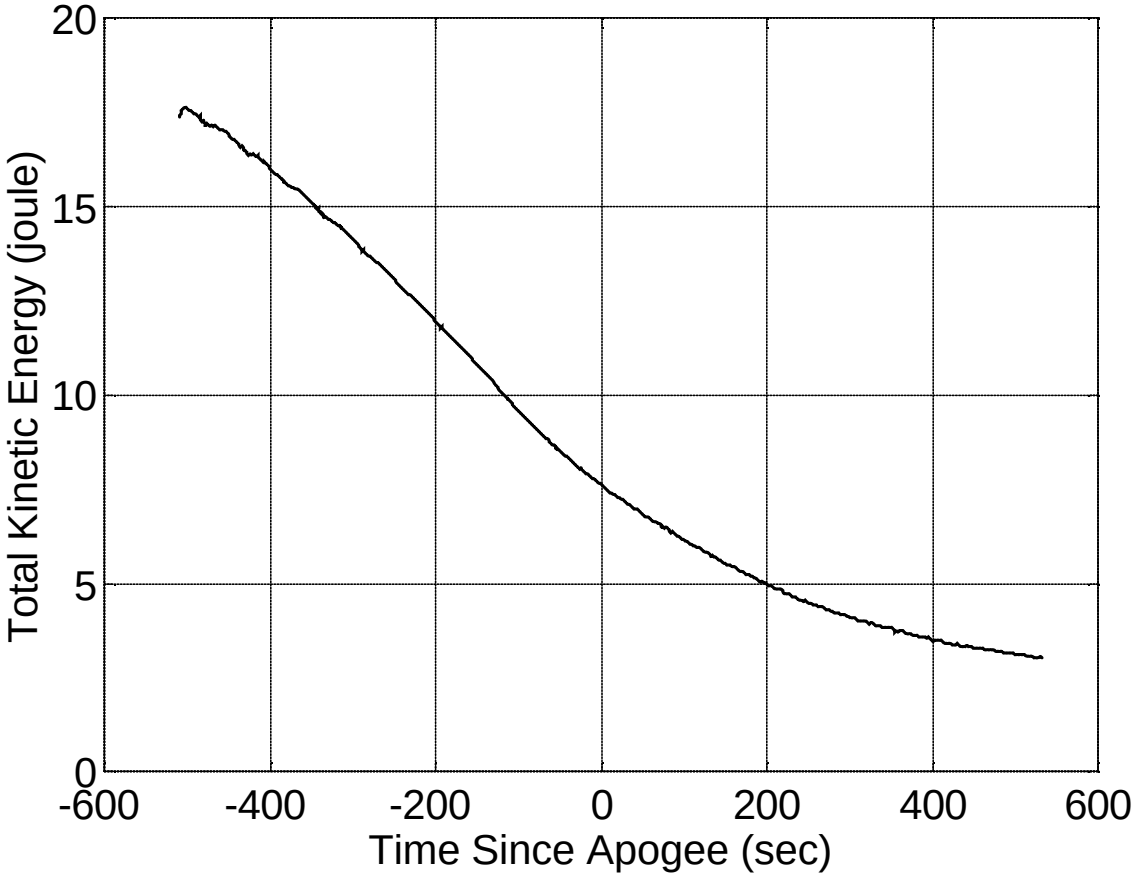

Fig. 7. Estimated total kinetic energy time history for the nominal smoother.

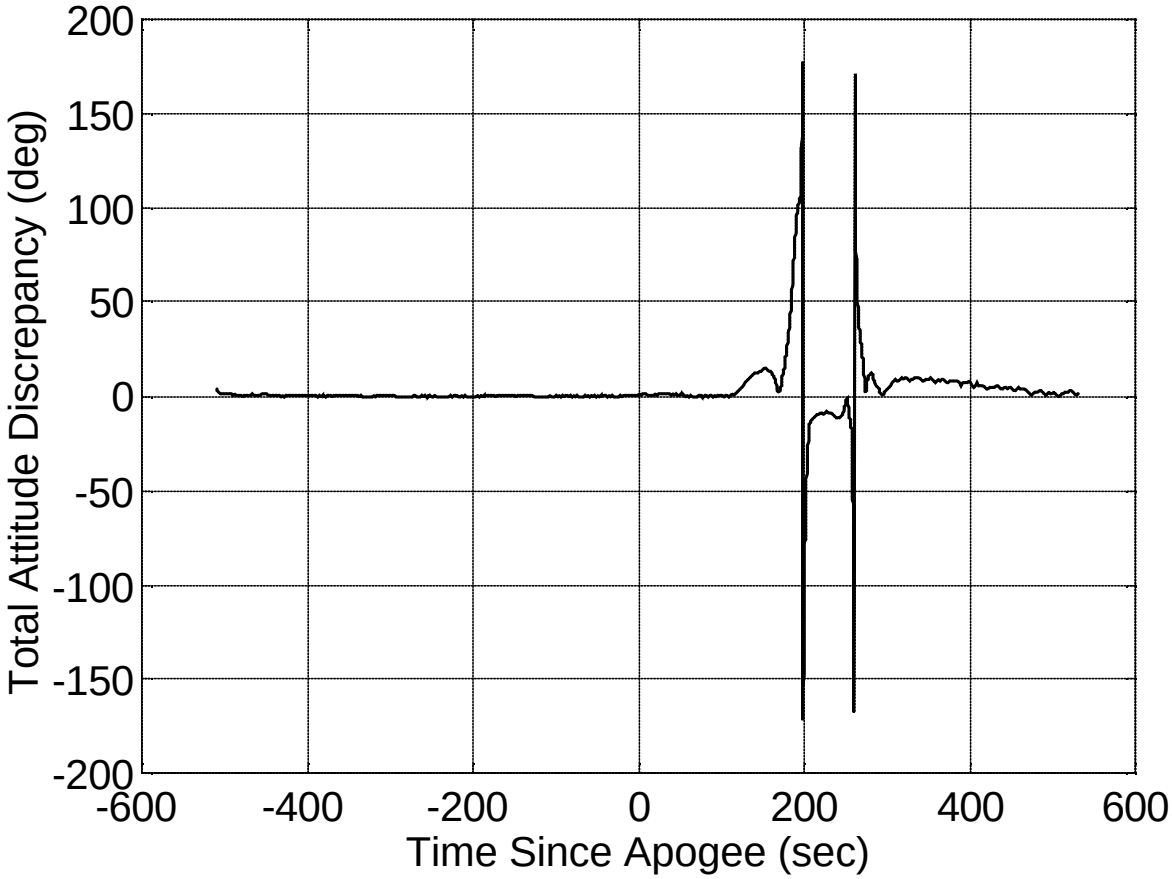

Fig. 8. Time history of the total attitude discrepancy between the nominal flexible-body smoother and the rigid-body smoother.